Title

Structure and Kinetic Engineering of Nanostructured Multi-Element Doped Ni-Rich Cathodes for Fast-Charging Lithium-ion Batteries

ISBN

9798190928877

Author

Shao, Yikun

Publication Date

2026-09-11

Peer reviewed|Thesis/dissertation

UNIVERSITY OF CALIFORNIA

Los Angeles

Structure and Kinetic Engineering of Nanostructured Multi-Element Doped Ni-Rich Cathodes for Fast-Charging Lithium-ion Batteries

A thesis submitted in partial satisfaction

of the requirements for the degree Master of Science

in Materials Science and Engineering

by

Yikun Shao

2026

ABSTRACT OF THE THESIS

Structure and Kinetic Engineering of Nanostructured Multi-Element Doped Ni-Rich Cathodes for Fast-Charging Lithium-ion Batteries

by

Yikun Shao

Master of Science in Materials Science and Engineering

University of California, Los Angeles, 2026

Professor Sarah H. Tolbert, Chair

Fast charging of Ni-rich layered oxide cathodes is limited by slow Li^+ transport and large structural changes at high states of charge. This thesis investigated nanostructuring and multi-element doping as a combined strategy for developing cobalt-free Ni-rich cathodes. NM-MgNbMo, NM-MgAlMo, and NM-MgTiNbMo were synthesized using a polymer-assisted micelle-templated sol–gel method and compared with bulk and less porous NMC-811. X-ray diffraction confirmed the layered α-$NaFeO_2$-type structure and distinct interlayer spacings; NM-MgNbMo had the least apparent cation mixing and largest spacing, supporting easier Li^+ transport and faster kinetics, while partial disorder may provide a stabilizing pillaring effect. NM-MgNbMo exhibited the best high-rate performance among the doped samples, maintaining approximately 36 mAh/g at 32C

when the capacity of bulk NMC-811 approached zero. CV and GITT measurements were also consistent with comparatively low apparent polarization for NM-MgNbMo. After 1000 cycles at 8C, NM-MgNbMo retained the highest absolute capacity, whereas NM-MgTiNbMo showed the highest fractional retention from a lower initial capacity. Operando X-ray diffraction showed substantially smaller c-lattice changes in the doped samples than in the NMC-811 references. Overall, NM-MgNbMo provided the best balance between high-rate capacity and structural stability, while NM-MgTiNbMo favored structural stability at the cost of accessible capacity.

This thesis of Yikun Shao is approved.

Alexander A. Balandin

Nathan Szymanski

Sarah H. Tolbert, Committee Chair

University of California, Los Angeles

2026

TABLE OF CONTENTS

LIST OF FIGURES

LIST OF TABLES

ACKNOWLEDGMENTS

I would first like to express my deepest gratitude to my parents, Yantao Shao and Qing Wang. Their continuous support, encouragement, and sacrifices made it possible for me to study overseas and complete my master's degree in Los Angeles. I could not have reached this stage without their trust and support.

I sincerely thank Professor Sarah Tolbert for giving me the opportunity to conduct research in her laboratory and for guiding me as my principal investigator. I am especially grateful to my mentor, Grace Kim, for patiently teaching me about experimental design, laboratory work, and data analysis throughout this project. Her guidance was essential to the completion of this thesis. I would also like to thank my subgroup members, Aina Sebastian, Becca McAlpine, Joeun Kim, and Miguel Reyna, for their help with data acquisition and experimental troubleshooting.

I am grateful to Professor Nathan Szymanski and Professor Alexander A. Balandin for serving on my thesis committee and for their time and consideration. Finally, I would like to thank my friend Ziyang Huang for discussing my research and writing with me and for providing helpful ideas during the revision of this thesis.

1. Introduction

Lithium-ion batteries (LIBs), advantageous for their high energy density, long cycle life, and high energy efficiency, are widely used in portable electronic devices, electric vehicles (EVs), and grid-scale energy storage.[1–5] Widespread EV adoption is slowed by long charging times and limited driving range, emphasizing the importance of designing fast-charging batteries without sacrificing driving range, cycle life, or safety.[6–9] Charging speed is constrained by the rate at which Li^+ moves through the electrolyte, across the electrode/electrolyte interface, and within the solid electrode. At high current, slow transport at any of these steps increases concentration gradients and polarization, which can accelerate heat generation and side reactions.[8–10] Tesla has developed liquid-cooled charging cables that circulate coolant to remove heat from the charging conductor and connector during high-current charging.[11] However, this charger-side thermal management does not eliminate Li^+ transport limitations within battery electrodes.[8–10] The central challenge is therefore to develop a high-capacity battery material capable of rapid Li^+ transport that remains stable during repeated high-rate cycling.

The family of nickel-rich layered transition-metal oxide cathodes, such as $LiNi_{0.8}Mn_{0.1}Co_{0.1}O_2$ (NMC-811), is widely used in commercial applications because it provides high operating voltage and high specific capacity.[12,13] NMC has an α-$NaFeO_2$-type structure, containing alternating layers of Li and a mixture of transition metals. NMC benefits from having cation substitution of Ni with Co and Mn because it allows their functions to be balanced. A high nickel content in NMC-811 is attractive because it provides a majority of the redox capacity but also increases cation mixing, a structural

defect where Ni^{2+} occupies Li sites, caused by Ni^{2+} and Li having similar ionic sizes. This Li^{+}/Ni^{2+} cation mixing reduces structural and thermal stability while slowing transport by blocking Li^{+} pathways.[2] Co and Mn serve to mitigate this issue by maintaining cation ordering and electronic transport.[2,14] Co also raises cost and supply-chain concerns because its resources are geographically concentrated in regions associated with human-rights concerns and political instability.[13,15] Consequently, a major materials-design goal is to replace Co with inexpensive, abundant elements while retaining the capacity and structural stability of a Ni-rich layered oxide.

Another limitation of Ni-rich NMC is its anisotropic lattice response during delithiation. The c-lattice first expands as Li^{+} is removed, but contracts sharply at high states of charge; repeated lattice breathing generates internal strain and can contribute to microcracking and capacity loss.[16,17] These effects become more severe at high voltage and high rate, making bulk Ni-rich materials difficult to charge rapidly while maintaining long-term stability.

Elemental substitution and other structural additives have been investigated to strengthen the oxide framework, suppress unfavorable phase transformations, and reduce strain accumulation in Ni-rich and Co-free layered cathodes.[15,18–20]

Recent work showed that multielement doping can improve structural stability and suppress strain during cycling. Zhang et al. reported the compositionally complex $LiNi_{0.8}Mn_{0.13}Ti_{0.02}Mg_{0.02}Nb_{0.01}Mo_{0.02}O_2$ cathode, which exhibited nearly zero volumetric change and retained approximately 85% of its capacity after 1000 cycles.[18] This result demonstrates that a compositionally complex dopant combination can reduce lattice strain

and improve long-term cycling stability.

Although the compositionally complex material showed strong cycling stability, the nominal composition does not identify the exact amount and atomic location of every dopant. In this thesis, the sol-gel route combines metal precursors at controlled nominal ratios, allowing the three dopant combinations to be compared systematically; however, final stoichiometry and site occupancy still require direct measurement. Lee et al. separately showed that electrochemically induced partial transition-metal occupancy in the Li layer can suppress abrupt c-lattice collapse.[16] The present samples develop disorder during synthesis and contain much lower nominal dopant fractions, so the same pillaring mechanism cannot be assumed. Whether partial disorder contributes to their structural stability is therefore a hypothesis tested in this thesis, not a conclusion from the compositionally complex doping paper. Long-term capacity retention alone also does not show whether useful capacity is accessible during fast charging.

A strategy to improve the charging speed of NMC is by nanostructuring. Conventional bulk Ni-rich cathodes are made of large, dense particles that produce long solid-state diffusion paths. Nanostructuring can shorten Li^+ diffusion distances and increase contact between the active material and electrolyte, improving the response at high current.[21–23] In a related Ni-rich $LiNi_{0.80}Co_{0.15}Al_{0.05}O_2$ (NCA) cathode, Basile et al. found that a moderate primary-particle size of approximately 300 nm provided higher fast-rate capacity than both bulk material and a smaller-particle sample, reaching 150 mAh g^{-1} at 16C.[22]

It can also increase the contribution from intercalation pseudocapacitance, a

Faradaic Li^+-storage process that is less limited by long-range solid-state diffusion than conventional battery-type insertion.[24–26] Basile et al. reported that the NCA reaction is mainly solid-solution-like, so a moderate decrease in particle size primarily shortens diffusion distances rather than removing a moving two-phase boundary.[22] High-voltage structural transitions can still limit Ni-rich layered oxides; therefore, pseudocapacitive behavior must be evaluated from scan-rate-dependent electrochemical data rather than assumed from particle morphology alone.[22,24–26]

The full nominal transition-metal compositions, normalized to $LiMO_2$, are $LiNi_{0.800}Mn_{0.190}Mg_{0.005}Nb_{0.0025}Mo_{0.0025}O_2$ (NM-MgNbMo), $LiNi_{0.800}Mn_{0.185}Mg_{0.005}Al_{0.005}Mo_{0.005}O_2$ (NM-MgAlMo), and $LiNi_{0.800}Mn_{0.1825}Mg_{0.005}Ti_{0.005}Nb_{0.005}Mo_{0.0025}O_2$ (NM-MgTiNbMo). A 7.5 mol% excess of Li precursor was used to compensate for Li loss during heating; this synthesis input does not establish a final $Li_{1.075}$ product stoichiometry.

This study combines nanostructuring and multi-element doping to develop Co-free Ni-rich layered cathodes for fast charging. Three materials—NM-MgNbMo, NM-MgAlMo, and NM-MgTiNbMo—were synthesized by a polymer-assisted micelle-templated sol–gel method. Bulk NMC-811 and less porous NMC-811 are the reference samples to determine whether improvement of the doped samples is limited to comparison with dense bulk particles. Bulk NMC-811 is the conventional dense-particle benchmark. The less porous NMC-811 reference is less open than the micelle-templated cathodes; because porosity was not quantified, this label is qualitative. X-ray diffraction and Rietveld refinement were used to examine the layered structure and cation disorder, while

scanning electron microscopy was used to evaluate particle morphology. Rate capability, long-term cycling, cyclic voltammetry, and galvanostatic intermittent titration measurements were used to compare electrochemical kinetics, and operando X-ray diffraction was used to follow c-lattice evolution during cycling. The working hypothesis is that nanostructuring with shorter Li^+ transport pathways improves the fast-charging response of the mixed-metal Co-free materials, while the dopant combinations and partial disorder may limit lattice collapse. The desired material should therefore balance high-rate capacity with long-term structural stability rather than maximize either capacity or cation ordering alone.

2. Experimental Methods

2.1 Materials

The following chemicals were purchased from manufacturers and used directly without further purification: triblock copolymer Pluronic F127 ($EO_{100}PO_{65}EO_{100}$ M_W = 12600 Da, BASF), Polypropylene glycol 400 (PPO, Alfa Aesar), Tetrahydrofuran (THF, Fisher Chemical), lithium nitrate (98%+, MilliporeSigma), nickel nitrate hexahydrate (Ni 19.8% min, Thermo Scientific), manganese nitrate tetrahydrate (98%, Alfa Aesar), magnesium nitrate hexahydrate (99.999%, Thermo Scientific), aluminium nitrate nonahydrate (99+%, Alfa Aesar), ammonium bis(oxalate)oxotitinate hydrate (99.998%, Alfa Aesar), ammonium niobate oxalate hydrate (99.99%, Sigma Aldrich), ammonium molybdate (para) tetrahydrate (99%, Thermo Scientific). For preparation of electrodes prior to assembling coin-type half-cells, the following chemicals were used: single-walled carbon nanotube (swCNT), polyvinylidene fluoride (PVDF), Super P (Alfa Aesar), 1-Methyl-2-pyrrolidinone (NMP, Thermo Scientific).

2.2 Synthesis and thermal treatment of NM-MgNbMo, NM-MgAlMo, and NM-MgTiNbMo

A polymer-assisted micelle-templated sol-gel method was used to synthesize nanostructured NM-MgNbMo. Stoichiometric amounts of $LiNO_3$, $Ni(NO_3)_2 \cdot 6H_2O$, $Mn(NO_3)_2 \cdot 4H_2O$, $Mg(NO_3)_2 \cdot 6H_2O$, $C_4H_4NNbO_9 \cdot xH_2O$, and $(NH_4)_6Mo_7O_{24} \cdot 4H_2O$ were dissolved in distilled water, resulting in a total transition metal molar concentration of 0.6M. For $LiNO_3$, a 7.5% excess amount was added to prevent lithium loss during the

calcining process. In a separate container, 6.4 wt% Pluronic F127 was dissolved in distilled water. Subsequently, 0.34 wt% PPO 400 (to promote micelle growth) and 18.2 wt% THF (to disrupt the micelles) were added to the F127 solution, and the mixture was stirred at 50–55 °C for 3 hours to remove the THF. The completely dissolved metal salts solution and the THF-free F127 solution were mixed and stirred continuously for another 2 hours. The mixed solution was then evenly distributed into multiple glass petri dishes and dried in an oven at 80°C. The dried powder was then placed in a ceramic boat and subjected to preheating in a tube furnace under a flow of oxygen at 180°C and 450°C (for 4 hours each) to remove residual water and the template. In the subsequent calcination process, the powder was subjected to a ramp rate reaching 850°C over 30 minutes, held at this temperature for 30 minutes, and then cooled to 700°C at the fastest cooling rate, where it was held for 12 hours. Once the temperature dropped naturally to 350°C, the powder was rapidly transferred into a glovebox to prevent contact with water in the air. NM-MgAlMo and NM-MgTiNbMo were synthesized by the same method but with some different chemicals such as $Al(NO_3)_3 \cdot 9H_2O$ and $(NH_4)_2TiO(C_2O_4) \cdot xH_2O$.

Sample	Ni	Mn	Mg	Al	Ti	Nb	Mo	Li
NM-MgNbMo	80%	19%	0.5%	—	—	0.25%	0.25%	107.5%
NM-MgAlMo	80%	18.5%	0.5%	0.5%	—	—	0.5%	107.5%
NM-MgTiNbMo	80%	18.25%	0.5%	—	0.5%	0.5%	0.25%	107.5%

Table 2.1: The stoichiometric ratios of the dopant elements for NM-MgNbMo, NM-MgAlMo, and NM-MgTiNbMo.

2.3 Materials characterization

X-ray diffraction was applied by using PANalytical X'Pert Pro X-ray Powder Diffractometer with Cu Kα source (λ = 1.5418 Å) under 45kV voltage and 40mA current. A zero-background sample holder was used to avoid background interference. Scanning electron microscopy was applied by using FEI Nova 230 NanoSEM with 10kV accelerating voltage and 5.5mm working distance.

2.4 Electrochemical characterization

The slurries of NM-MgNbMo, NM-MgAlMo, and NM-MgTiNbMo were made in Argon atmosphere glovebox with composition of 90 wt% active material, 5 wt% PVDF, 4 wt% Super P, and 1 wt% swCNT. The slurries were cast evenly onto carbon-coated aluminum foil using the doctor-blade method. Then, they were vacuum-dried overnight at 120°C in heated antechamber of glovebox. The dried slurries were punched into electrodes with an area of 0.7 cm^2. CR 2032 type coin cells were assembled with positive electrodes, Celgard 2325 separator, Lithium metal (reference electrode), and electrolyte (solution of 1M $LiPF_6$ with 1:1:1 ratio of EC:DMC:DEC). Galvanostatic charge-discharge tests were conducted on Landt Battery Test System with constant current under voltage window of 2.7-4.2 V vs. Li/Li^+. The C-rate range of tests was from C/10 to 64C (1C = 160 mAh/g). Before the rate-capability and long-term cycling tests, the cells underwent formation cycling at C/10. Cyclic voltammetry (CV) test was conducted on BioLogic VSP Potentiostat with a range of scan rate from 0.1 to 1.0 mV/s under voltage window of 2.7-4.2 V vs. Li/Li^+. Galvanostatic intermittent titration technique (GITT) was also conducted on Landt Battery Test System by (dis)charging for 15 minutes at a current density of C/10

and then having a 2-hour rest.

2.5 *Operando* X-ray Diffraction characterization

Operando X-ray diffraction measurements were performed at beamline 11-3 of the Stanford Synchrotron Radiation Lightsource (SSRL) to monitor structural evolution during electrochemical cycling. Electrodes of NM-MgNbMo, NM-MgTiNbMo, bulk NMC-811, and less porous NMC-811 were assembled into pouch-type half-cells using lithium metal as the counter/reference electrode and a glass-fiber separator. The electrolyte described in Section 2.4 was added in an amount sufficient to wet the separator. An otherwise identical blank pouch cell without an active-material slurry coating was measured, and its diffraction pattern was used for background subtraction. Before the operando measurement, one formation cycle was conducted at 0.1C using a BioLogic VSP potentiostat within a voltage window of 2.7–4.2 V vs. Li/Li^+. During operando XRD acquisition, all four cells were charged at 0.2C within the same voltage window. Data collection for NM-MgNbMo and NM-MgTiNbMo continued through the subsequent discharge, whereas bulk NMC-811 and less porous NMC-811 were monitored during the charging portion only. The diffraction data were processed using GSAS-II[27] and integrated to obtain operando XRD patterns, which were presented as heat maps. The position of the (003) reflection was tracked and fitted to determine the c-lattice parameter as a function of cell voltage.

3. Results and Discussion

3.1 Structural and Morphological Characterization

3.1.1 Scanning Electron Microscopy (SEM) characterization

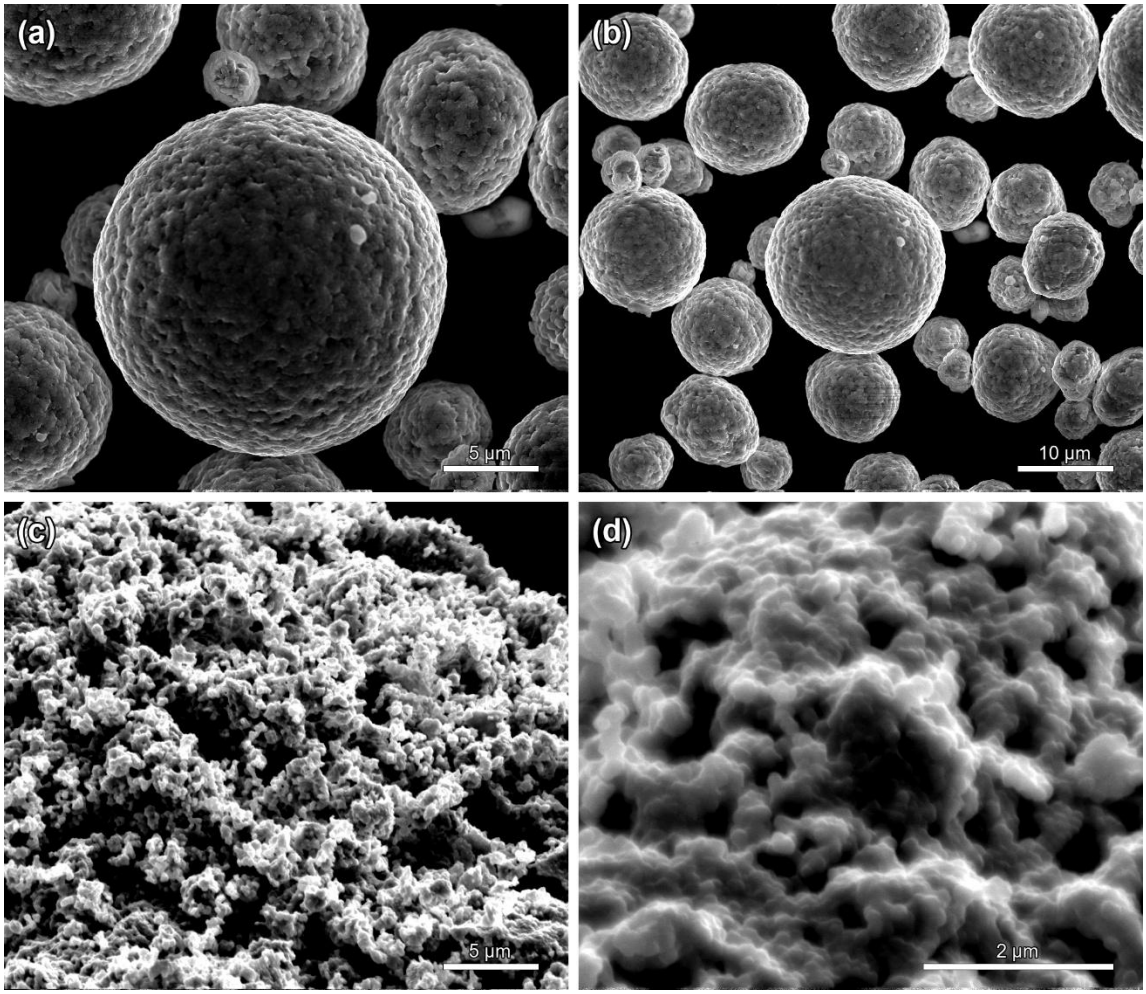

Figure 3.1: SEM images of bulk NMC-811 at (a) 10,000× and (b) 5,000× magnification, and NM-MgNbMo at (c) 10,000× and (d) 50,000× magnification. Scale bars are 5, 10, 5, and 2 µm, respectively.

Scanning electron microscopy (SEM) was used to compare NM-MgNbMo with bulk NMC-811, which serves as a conventional dense-particle reference (Figure 3.1). Figures 3.1(a) and 3.1(b) show that bulk NMC-811 consists mainly of micrometer-scale, nearly spherical secondary particles. Their clear boundaries and relatively compact

surfaces are consistent with substantial consolidation of the primary grains.

In contrast, NM-MgNbMo in Figure 3.1(c) exhibits an irregular, more open agglomerated morphology. The higher-magnification image in Figure 3.1(d) resolves interconnected primary grains, necking between neighboring grains, and open gaps throughout the particle network. These features indicate that calcination produced grain growth and partial coarsening without complete consolidation into dense spherical secondary particles. The retained open texture is qualitatively consistent with removal of the F127 template during heating.

Compared with bulk NMC-811, NM-MgNbMo therefore has a less consolidated network of interconnected primary grains and open gaps. This morphology may shorten particle-scale Li^+ transport distances and increase the accessible surface area relative to compact bulk particles.[21–23]

3.1.2 X-ray diffraction (XRD) characterization

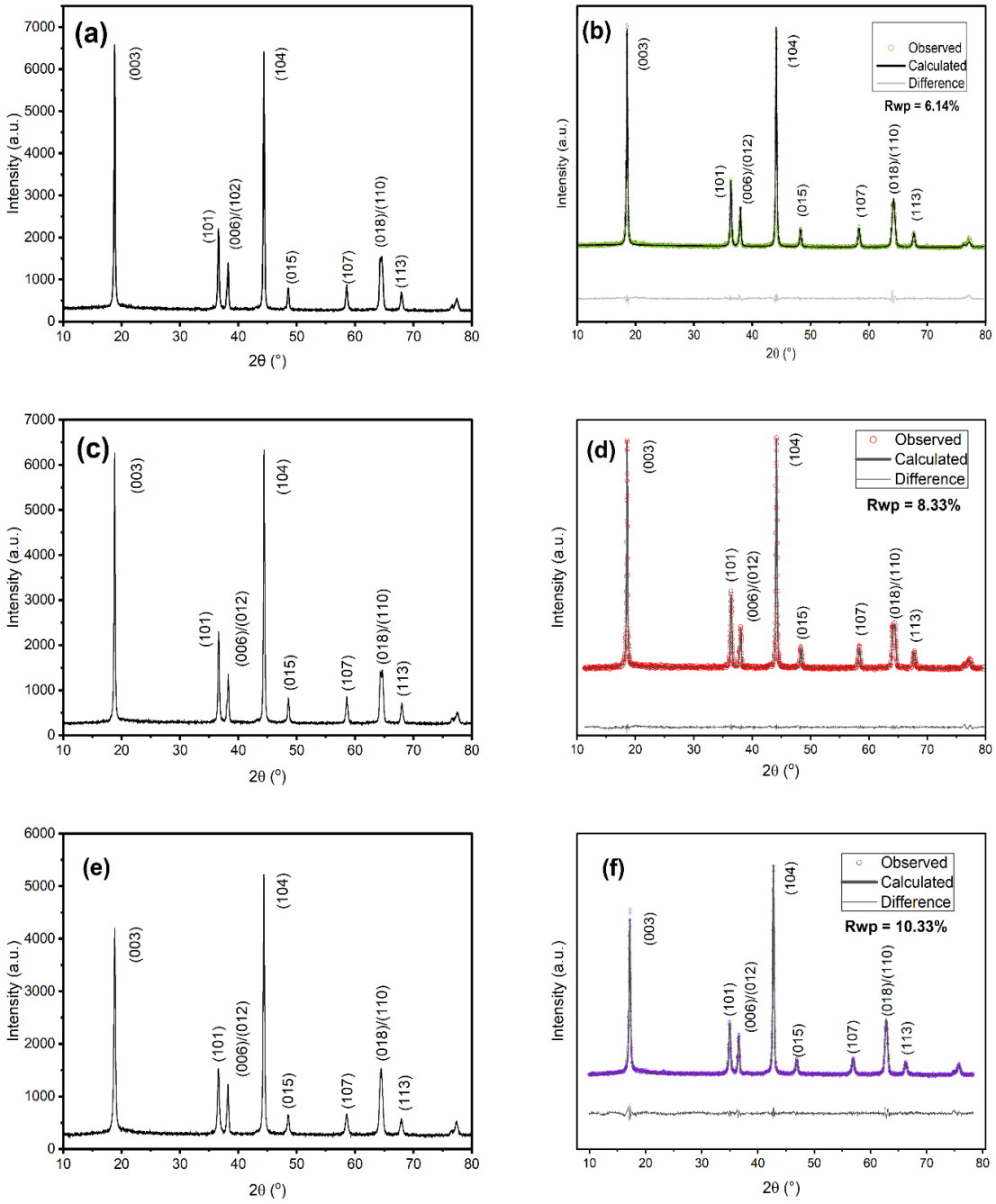

Figure 3.2: XRD patterns (a, c, e) and Rietveld refinement profiles (b, d, f) for NM-MgNbMo (a, b), NM-MgAlMo (c, d), and NM-MgTiNbMo (e, f). Reflections are indexed to the layered α-$NaFeO_2$-type R-3m structure. The corresponding Rwp values are 6.1%, 8.3%, and 10.3%, respectively.

Powder X-ray diffraction (XRD) and Rietveld refinement were used to evaluate the phase purity and average layered structure of NM-MgNbMo, NM-MgAlMo, and NM-MgTiNbMo. As shown in Figure 3.2(a, c, and e), all three samples exhibit the characteristic reflections of the layered α-$NaFeO_2$-type structure with the R-3m space group. No obvious impurity peaks are detected, indicating that a dominant layered phase was obtained without a detectable large fraction of crystalline secondary phases. The calculated profiles in Figure 3.2(b, d, and f) reproduce the main features of the observed patterns, supporting use of the refined lattice parameters for the following structural comparison.

The I(003)/I(104) integrated peak-area ratio is a qualitative indicator of Li^+/Ni^{2+} cation mixing; values below 1.2 indicate greater mixing in layered Ni-rich oxides.[28] The measured ratios are 0.96 for NM-MgNbMo, 0.95 for NM-MgAlMo, and 0.86 for NM-MgTiNbMo. Because octahedral Ni^{2+} (0.69 Å) is similar in size to Li^+ (0.76 Å), some Ni^{2+} can occupy Li sites during synthesis.[28] All three samples therefore show apparent disorder, ranked NM-MgTiNbMo > NM-MgAlMo > NM-MgNbMo.

The nominal total dopant contents are only 1.0 mol% for NM-MgNbMo, 1.5 mol% for NM-MgAlMo, and 1.75 mol% for NM-MgTiNbMo, compared with 7 mol% in the compositionally complex material reported by Zhang et al.[18] Their sub-1.2 ratios show that partial disorder can form under the present sol-gel synthesis even at much lower dopant contents.

Partial disorder is a design feature rather than only a defect. Controlled transition-metal occupancy in the Li layer can support adjacent oxygen slabs through a pillaring

effect and suppress c-lattice collapse, whereas excessive cation mixing can block Li^+ pathways and reduce accessible capacity.[16] The desired structure therefore balances enough disorder for structural support with open Li^+ pathways.

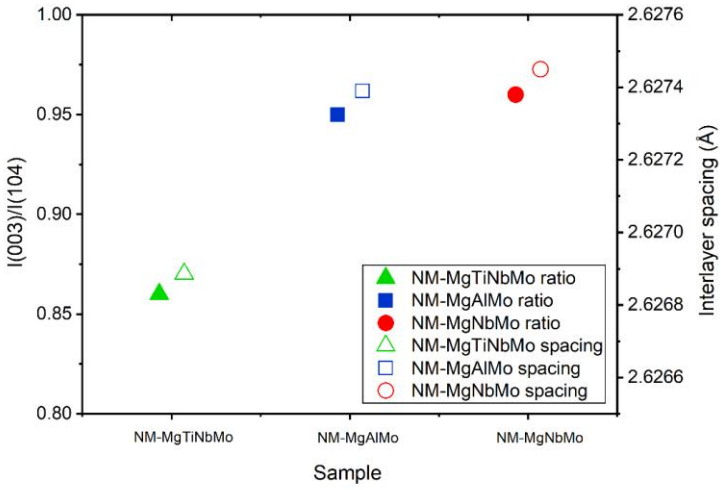

Figure 3.3: I(003)/I(104) ratios (filled symbols; left axis) and calculated Li-layer spacings (open symbols; right axis) for the three doped samples.

Rietveld refinement can quantify cation mixing when the Li/Ni site occupancies are refined. Here, the Ni occupancy on the Li site was fixed at 0.03, so the I(003)/I(104) ratio was used to compare the samples. The refined c-lattice parameter and the fixed oxygen z-coordinate ($Zox = 0.259$) from the starting CIF were used to calculate the transition-metal-oxide slab spacing (S) and Li-layer interlayer spacing (I):

$$S = 2\left(\frac{1}{3} - Zox\right)c$$

$$I = \frac{c}{3} - S$$

where S is the slab spacing, I is the interlayer spacing, c is the c-lattice parameter, and Zox is the oxygen z-coordinate. A larger interlayer spacing means a wider Li^+ migration layer for easier transportation and faster kinetics.[28] The calculated values are 2.62745 Å for

NM-MgNbMo, 2.62739 Å for NM-MgAlMo, and 2.62689 Å for NM-MgTiNbMo. The values are different and follow the same order as I(003)/I(104): NM-MgNbMo > NM-MgAlMo > NM-MgTiNbMo. Thus, less apparent cation mixing is associated with larger Li-layer interlayer spacing in this dataset.

All three samples retain the targeted layered phase but differ in apparent cation mixing and Li-layer interlayer spacing. NM-MgNbMo has the least apparent mixing and the largest spacing, providing the most open Li^+ transport layer for easier transportation and faster kinetics. NM-MgTiNbMo has the greatest apparent mixing and the smallest spacing. These results identify partial disorder as the key balance: enough transition-metal occupancy may provide a stabilizing pillaring effect, while limited mixing preserves interlayer space for Li^+ transport. This disorder-spacing relationship is a finding of the present thesis and was not established in the high-entropy study by Zhang et al.[18]

3.2 Electrochemical & kinetic performance

3.2.1 Galvanostatic voltage (GV) behavior

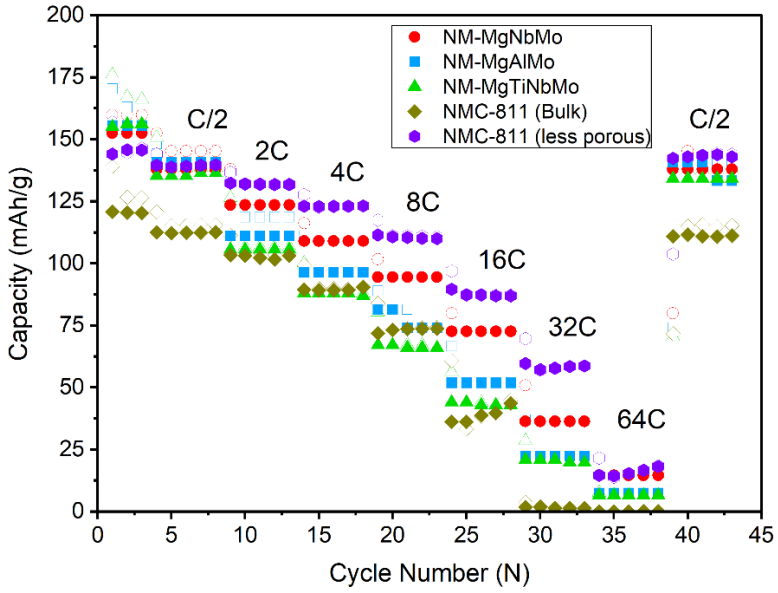

Figure 3.4: Discharge capacity of NM-MgNbMo, NM-MgAlMo, NM-MgTiNbMo, bulk NMC-811, and less porous NMC-811 during stepwise rate testing from C/2 to 64C, followed by recovery at C/2.

Galvanostatic charge–discharge measurements were used to compare the rate capability of the three Co-free doped cathodes with bulk and less porous NMC-811. Bulk NMC-811 consists of dense secondary particles and is expected to have longer particle-scale Li^+ transport pathways than the more open synthesized materials. At high current, these longer pathways produce larger Li^+ concentration gradients and stronger polarization, which is consistent with the bulk sample showing the slowest high-rate response. Nanostructuring can shorten solid-state diffusion distances and improve rate capability.[22] The less porous NMC-811 sample provides an undoped reference with lower apparent porosity than the micelle-templated powders. After formation cycling at C/10, the rate test in Figure 3.4 was increased stepwise from C/2 to 64C and then returned to C/2. The final C/2 step evaluates how much of the high-rate capacity loss is recovered

after the current is reduced.

All materials lose discharge capacity as the rate increases. Less porous NMC-811 gives the highest capacity through most of the rate sequence, whereas the doped samples perform better than bulk NMC-811 at high rates. At 32C, NM-MgNbMo retains approximately 36 mAh/g, while bulk NMC-811 approaches zero capacity. NM-MgNbMo also gives the highest capacity among the doped samples from 8C to 64C. However, none of the doped materials surpasses the less porous reference. This result is reasonable because replacing some redox-active Ni with dopants can lower the available capacity, while transition-metal occupancy in the Li layer can reduce the number of unobstructed Li^+ pathways.[28]

At 32C and 64C, the large capacity loss of all samples shows that extreme current densities still impose strong kinetic limitations. When the rate returns to C/2, the three doped samples recover to approximately 133–138 mAh/g, compared with about 143 mAh/g for less porous NMC-811 and 111 mAh/g for bulk NMC-811. This recovery indicates that much of the high-rate capacity loss is reversible, although it does not rule out structural degradation. Partial cation disorder also creates an expected trade-off: a transition-metal ion in the Li layer can obstruct a local Li^+ channel and lower short-term capacity, but it may also constrain slab motion and improve structural stability.[16,28] Therefore, the intended benefit of pillaring is not necessarily higher rate capacity than the undoped reference, but better retention during repeated cycling. The 8C cycling test was used to evaluate this proposed stability benefit.

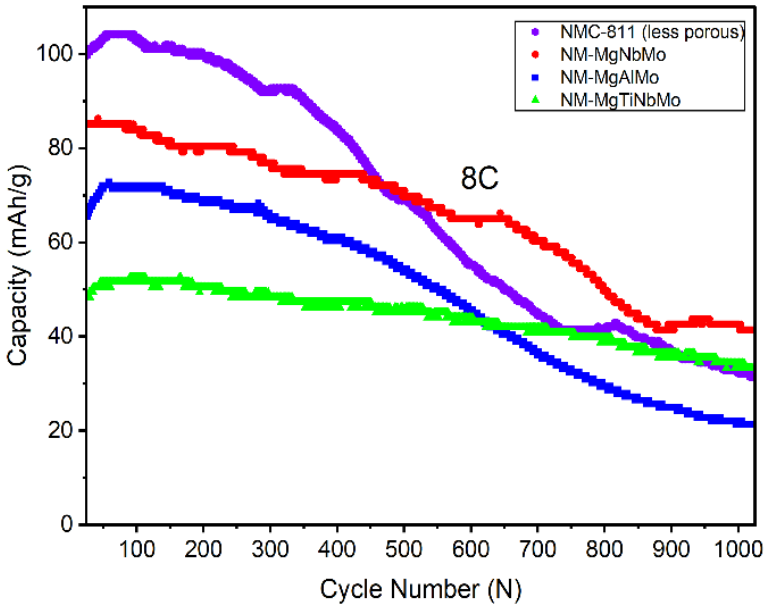

Figure 3.5: Long-term cycling performance at 8C of NM-MgNbMo, NM-MgAlMo, NM-MgTiNbMo, and less porous NMC-811 over 1000 cycles.

Figure 3.5 compares the 8C cycling behavior over 1000 cycles. Less porous NMC-811 decreases from approximately 100 to 30 mAh/g. NM-MgNbMo decreases from about 85 to 42 mAh/g, NM-MgAlMo from about 70 to 21 mAh/g, and NM-MgTiNbMo from about 50 to 32 mAh/g. NM-MgNbMo therefore retains the highest absolute capacity after 1000 cycles. Because the samples begin at different capacities, the retention fraction is also needed for a fair comparison.

Based on the approximate values in Figure 3.5, NM-MgTiNbMo retains about 64% of its initial capacity, compared with approximately 49% for NM-MgNbMo and 30% for both NM-MgAlMo and less porous NMC-811. The high fractional retention of NM-MgTiNbMo is offset by its lower initial and final capacities. The relationship to the XRD results is notable: NM-MgTiNbMo shows the greatest apparent cation disorder and the highest fractional retention, whereas NM-MgNbMo combines lower apparent disorder with the highest final capacity. NM-MgAlMo does not show a retention advantage over

less porous NMC-811, indicating that the presence of dopants alone is not sufficient to improve cycling stability.

The cycling trends are consistent with, but do not directly prove, a pillaring contribution from partial cation disorder. In a related Co-free Ni-rich layered oxide, controlled partial cation disorder was reported to suppress lattice collapse and improve cycle life.[16] Compositionally complex doping and Ti incorporation have also been reported to reduce structural degradation in Ni-rich layered cathodes.[18,29] In the present study, the better retention of NM-MgNbMo and NM-MgTiNbMo relative to less porous NMC-811 supports the proposed connection between structural constraint and cycling stability. However, the I(003)/I(104) ratio is only a qualitative indicator of cation disorder and cannot identify which cations occupy Li-layer sites. Differences in dopant chemistry and particle morphology also contribute, so the GV data cannot establish the pillaring mechanism by themselves.

Overall, less porous NMC-811 remains the strongest capacity benchmark during the rate test. Among the doped materials, NM-MgNbMo gives the best balance of rate capability and long-term capacity, with the highest high-rate response and the highest absolute capacity after 1000 cycles. NM-MgTiNbMo shows the highest fractional retention but at lower accessible capacity. The GV results therefore show a capacity–stability trade-off: open Li^+ pathways favor accessible capacity and rate response, whereas partial structural constraint may improve durability during repeated high-rate cycling.

3.2.2 Cyclic voltammetry (CV) behavior

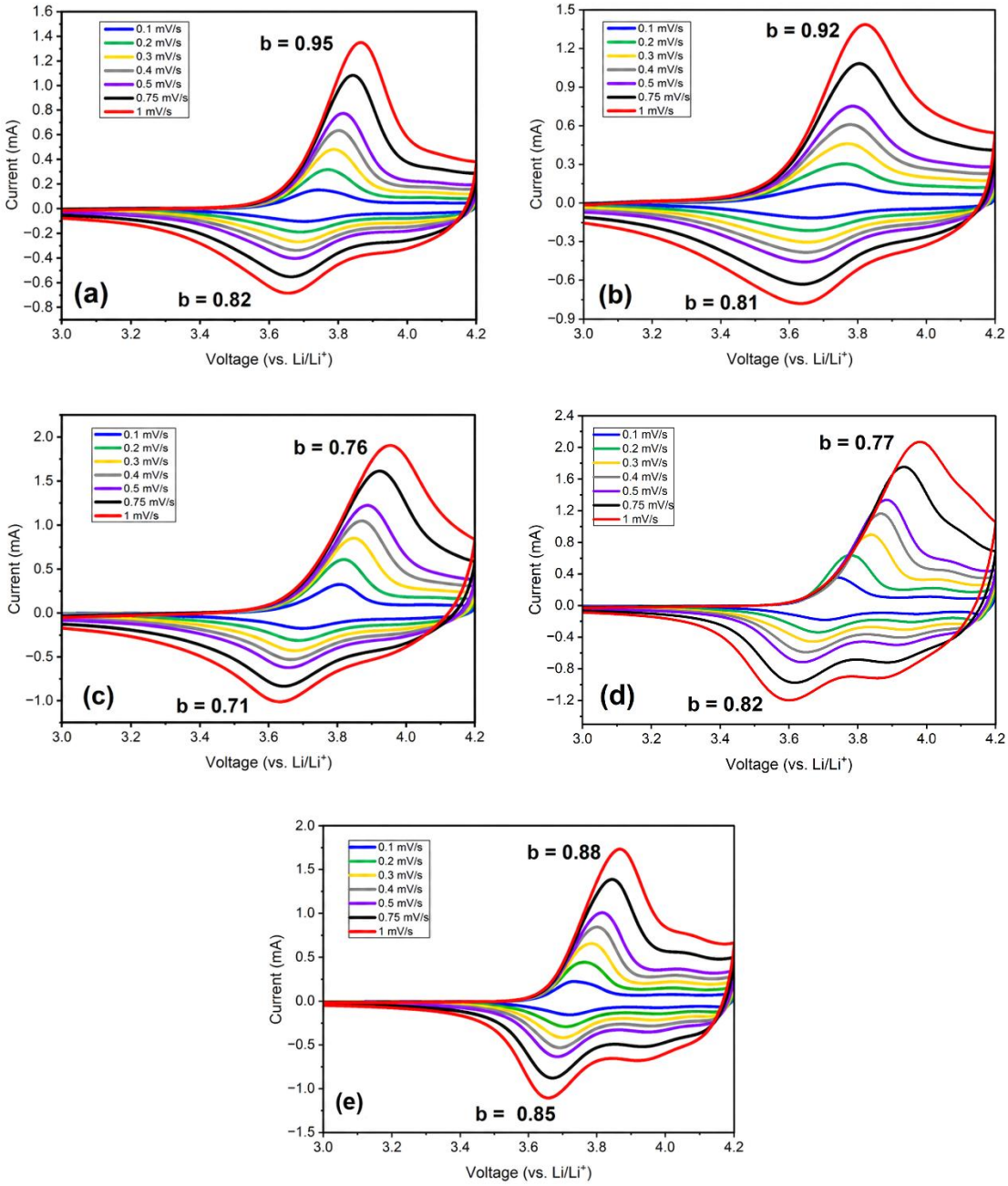

Figure 3.6: Cyclic voltammetry curves recorded at scan rates from 0.1 to 1.0 mV/s and the corresponding anodic and cathodic b-values for (a) NM-MgNbMo, (b) NM-MgAlMo, (c) NM-MgTiNbMo, (d) bulk NMC-811, and (e) less porous NMC-811.

Cyclic voltammetry (CV) was used to compare the reaction kinetics of NM-MgNbMo, NM-MgAlMo, NM-MgTiNbMo, bulk NMC-811, and less porous NMC-811.

Measurements were collected between 2.7 and 4.2 V vs. Li/Li^+ at scan rates of 0.1–1.0 mV/s (Figure 3.6). Each sample shows a broad anodic-cathodic peak pair that is mainly associated with Ni redox and the accompanying evolution of the layered structure.[2,14] With increasing scan rate, the anodic peak shifts to higher potential and the cathodic peak shifts to lower potential. The increasing peak separation indicates that kinetic polarization becomes larger when less time is available for charge transfer and Li^+ transport.

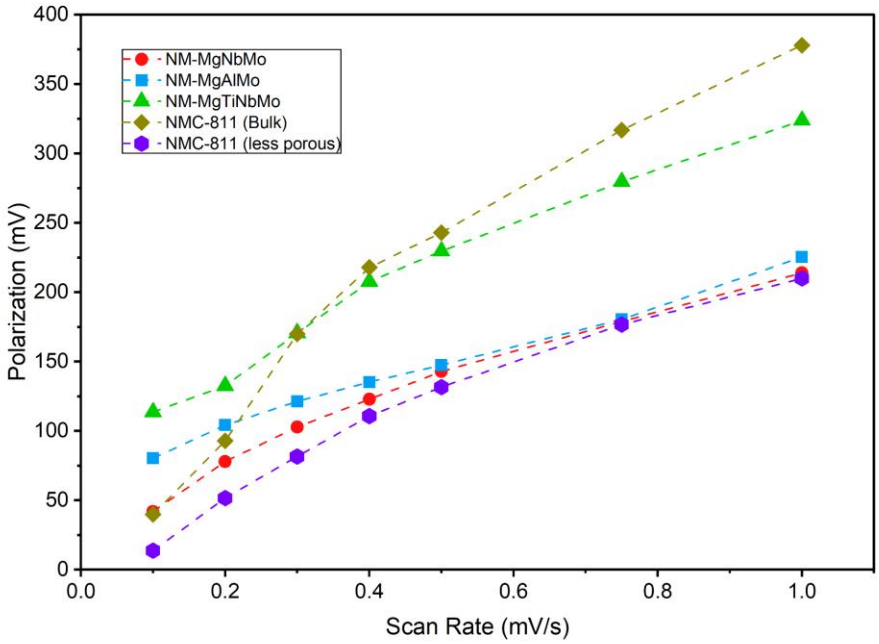

Figure 3.7: Apparent CV polarization, calculated from the anodic-cathodic peak-potential separation, as a function of scan rate for NM-MgNbMo, NM-MgAlMo, NM-MgTiNbMo, bulk NMC-811, and less porous NMC-811.

For comparison, apparent CV polarization was defined as the separation between the anodic and cathodic peak potentials, $\Delta E_p = E_{pa} - E_{pc}$ (Figure 3.7). Because peak separation includes ohmic, charge-transfer, and Li^+-transport contributions, it is used as a comparative kinetic metric rather than a single measured overpotential. The value

increases with scan rate for all five materials. Less porous NMC-811 increases from approximately 15 to 210 mV. Among the doped cathodes, NM-MgNbMo increases from about 40 to 215 mV, NM-MgAlMo from about 80 to 225 mV, and NM-MgTiNbMo from approximately 115 to 325 mV. Bulk NMC-811 begins near 40 mV but rises most strongly to approximately 380 mV at 1.0 mV/s. Thus, NM-MgNbMo has the lowest peak separation among the doped samples, although less porous NMC-811 remains the lowest-polarization reference.

The scan-rate dependence of the peak current was further analyzed using the power-law relationship:

$$i = av^b$$

where i is the absolute peak current, v is the scan rate, and a and b are constants. The b-value is obtained from the slope of $\log(i)$ versus $\log(v)$. For a semi-infinite diffusion-controlled response, b approaches 0.5, whereas a current response proportional to scan rate gives b close to 1. Values between these limits indicate mixed kinetic contributions. A b-value near 1 is consistent with a response that is less limited by long-range solid-state diffusion and can include intercalation pseudocapacitance, but it does not by itself prove that all stored charge is pseudocapacitive.[22,24,30]

The extracted b-values show that delithiation and lithiation do not have identical rate dependence. NM-MgNbMo has anodic and cathodic values of 0.95 and 0.82, respectively, while NM-MgAlMo gives 0.92 and 0.81. Their anodic values near 1 are consistent with strong near-surface or short-diffusion-length contributions during delithiation. NM-MgTiNbMo gives lower values of 0.76 and 0.71, indicating a greater

dependence on solid-state Li^+ diffusion. Bulk NMC-811 has values of 0.77 and 0.82, whereas less porous NMC-811 gives 0.88 and 0.85. The less porous reference combines relatively high *b*-values with the smallest peak separation. In contrast, the lower anodic *b*-value and rapidly increasing peak separation of bulk NMC-811 indicate stronger transport limitations during delithiation at high scan rates.

These results connect the CV analysis to the pseudocapacitance discussed in the introduction. The high anodic *b*-values of NM-MgNbMo and NM-MgAlMo are consistent with intercalation pseudocapacitance or near-surface charge storage during delithiation. Nanostructuring may support this response by shortening Li^+ diffusion distances, as reported for nanostructured NCA.[22] Although the *b*-values provide information about the scan-rate dependence of the electrochemical response, they do not quantify the relative capacitive and diffusion-controlled contributions. Therefore, the present CV results are interpreted as a comparative kinetic analysis. Among the doped materials, NM-MgNbMo shows the most favorable combined CV response because it has a high anodic *b*-value and the smallest peak separation.

3.2.3 Galvanostatic intermittent titration technique (GITT) behavior

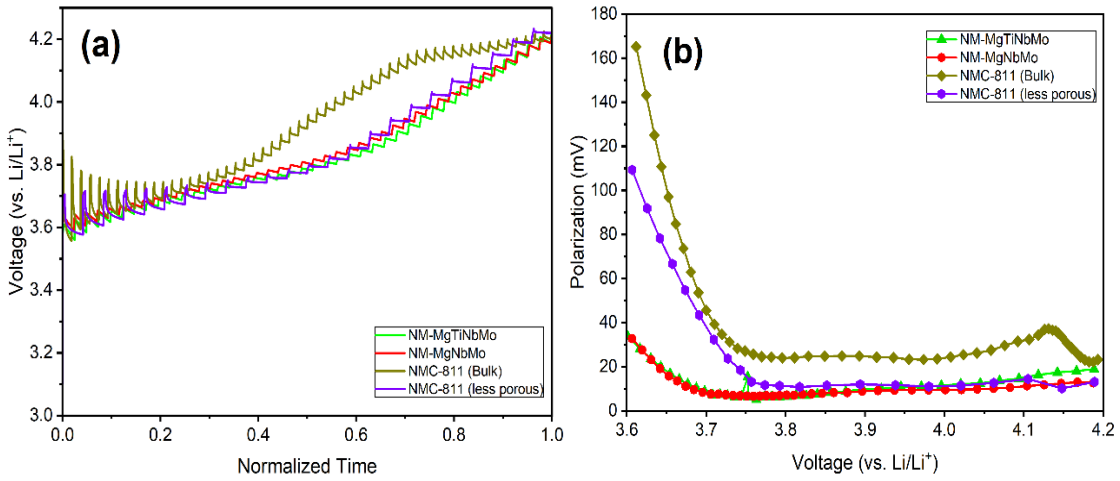

Figure 3.8: First-charge GITT voltage profiles plotted against normalized time and corresponding apparent pulse-relaxation polarization for NM-MgNbMo, NM-MgTiNbMo, bulk NMC-811, and less porous NMC-811

Galvanostatic intermittent titration technique (GITT) is commonly used to estimate the chemical Li^+ diffusion coefficient from the voltage response to a small current pulse. Conventional analysis assumes diffusion-controlled behavior, a representative particle geometry and diffusion length, a sufficiently small perturbation, and relaxation close to equilibrium.[31] These assumptions are difficult to verify for the micelle-templated composite electrodes used here because their active surface area and effective diffusion length are not known. Therefore, Li^+ diffusion coefficients are not reported. Instead, the pulse and relaxation responses are compared using an apparent polarization metric. NM-MgAlMo was excluded because abnormal voltage fluctuations made its extracted values unreliable.

Figure 3.8(a) presents the first-charge voltage profiles on a common normalized-time scale. Each C/10 current pulse causes an upward voltage step as Li^+ is extracted, followed by a downward relaxation toward a quasi-equilibrium value during the 2 h rest. In Figure 3.8(b), the apparent pulse-relaxation polarization was calculated as $\Delta V =$

$|V_{end,pulse} - V_{relaxed}|$. A larger ΔV means that the electrode was driven farther from quasi-equilibrium during the pulse and underwent a larger relaxation, indicating stronger combined ohmic, charge-transfer, and concentration polarization. A smaller ΔV indicates lower overall kinetic polarization, but it does not identify which contribution is rate limiting.

The apparent polarization is largest at the beginning of charge. Near full lithiation, the Li layers contain few vacant sites, so the lower-barrier divacancy-mediated Li^+ hopping pathway is less available. As delithiation creates vacancies, Li^+ transport becomes less restricted.[32] Bulk and less porous NMC-811 initially show apparent polarization values of approximately 160 and 110 mV, respectively, compared with about 30–35 mV for NM-MgNbMo and NM-MgTiNbMo. Between approximately 3.75 and 4.00 V, the values decrease to about 20–25 mV for bulk NMC-811, 10–15 mV for less porous NMC-811, and mostly below 15 mV for the two doped samples. The lower values of the doped cathodes are consistent with shorter particle-scale transport paths that reduce Li^+ concentration gradients during each pulse.[21–23] The proposed partial-disorder/pillaring structure may also constrain local slab rearrangement during delithiation,[16,18] although GITT cannot separate this structural contribution from morphology and charge-transfer effects. The lower apparent polarization is consistent with the favorable high-rate and long-term cycling trends of NM-MgNbMo and NM-MgTiNbMo, but it does not establish their cause.

Above 4.0 V, NM-MgNbMo, NM-MgTiNbMo, and less porous NMC-811 show similar apparent polarization values of approximately 10–18 mV, whereas bulk NMC-811

reaches about 35 mV near 4.13 V. Their lower response relative to the dense bulk sample is consistent with a beneficial morphology effect from shorter particle-scale transport pathways.[21–23] Because a validated diffusion model was not applied, these results are interpreted as a comparative kinetic metric rather than as Li^+ diffusion coefficients or evidence for a single controlling mechanism.

3.3 *Operando* XRD measurements

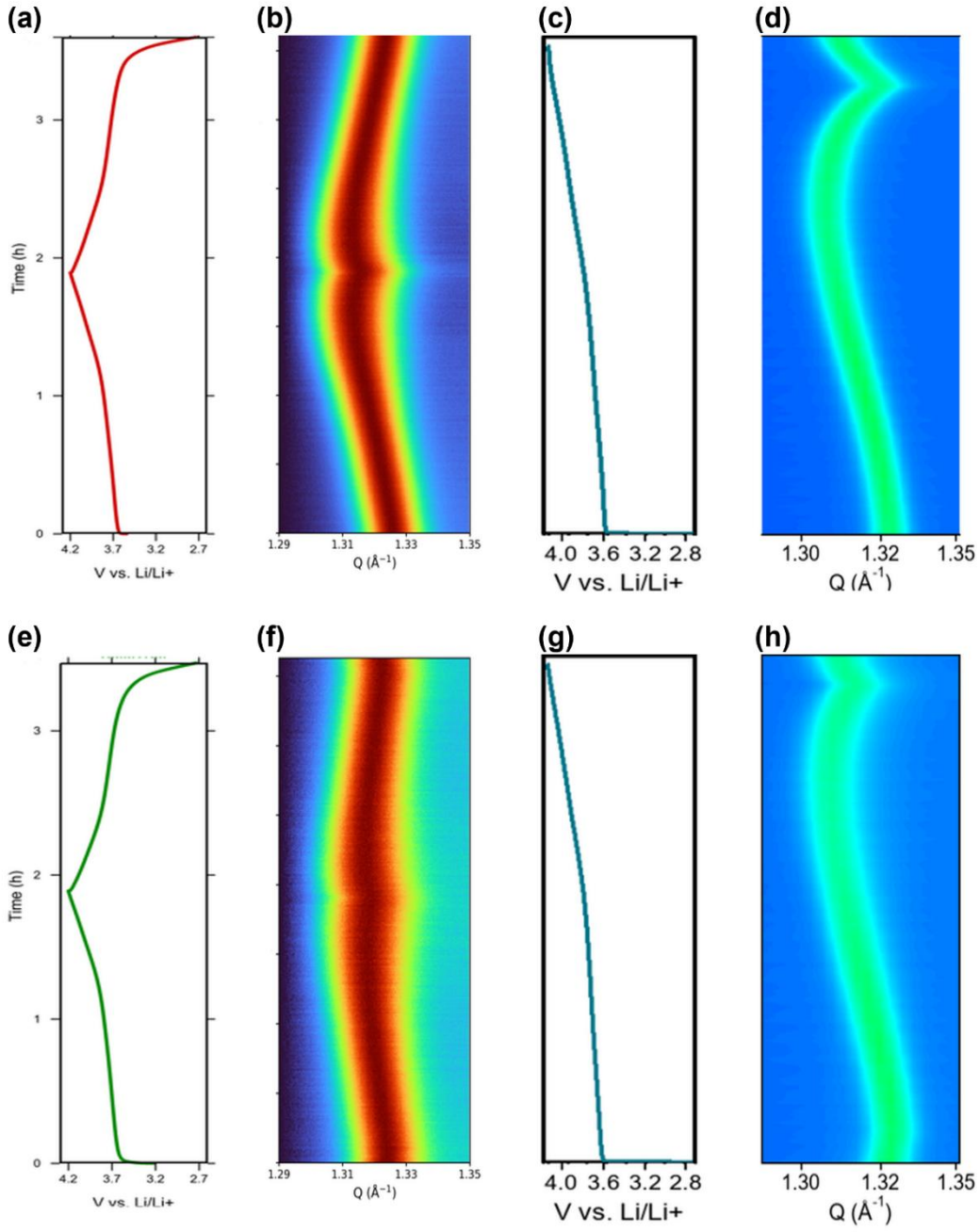

Figure 3.9: Operando voltage profiles and corresponding (003) XRD heat maps for (a, b) NM-MgNbMo, (c, d) bulk NMC-811, (e, f) NM-MgTiNbMo, and (g, h) less porous NMC-811. Panels (a, c, e, g) show the voltage profiles, while panels (b, d, f, h) show the corresponding heat maps.

Operando X-ray diffraction was used to compare the structural responses of the four cathodes. Figure 3.9 pairs each voltage profile with its (003) heat map. NM-MgNbMo and NM-MgTiNbMo were followed through one charge–discharge cycle after formation,

whereas the bulk and less porous NMC-811 data cover charge only. Therefore, reversibility is evaluated only for the doped samples. For the layered structure, d(003) = c/3 and Q = 2π/d, so lower Q indicates c-lattice expansion and higher Q indicates contraction. Here, state of charge (SOC) refers to the extent of delithiation during charge; higher SOC means greater Li removal.

During the early and middle stages of charging, the (003) reflections shift toward lower Q because Li^+ removal reduces electrostatic screening between adjacent oxygen layers, increasing oxygen–oxygen repulsion and expanding the interlayer spacing. Near the end of charge, the direction reverses. At high SOC, continued nickel oxidation contracts the transition-metal–oxygen layer, while charge transfer between O 2p and partially filled Ni 3d states decreases oxygen–oxygen repulsion across the Li layer. This electronic and structural evolution is associated with an H2–H3-type response around 4.2 V and contracts the c axis, shifting the (003) reflection back toward higher Q.[2,17,33] This reversal is strongest for bulk NMC-811, smaller for less porous NMC-811, and weaker for the doped samples. During discharge, the doped-sample peaks return toward their starting positions, indicating a largely reversible c-lattice response. NM-MgTiNbMo shows the smallest overall displacement.

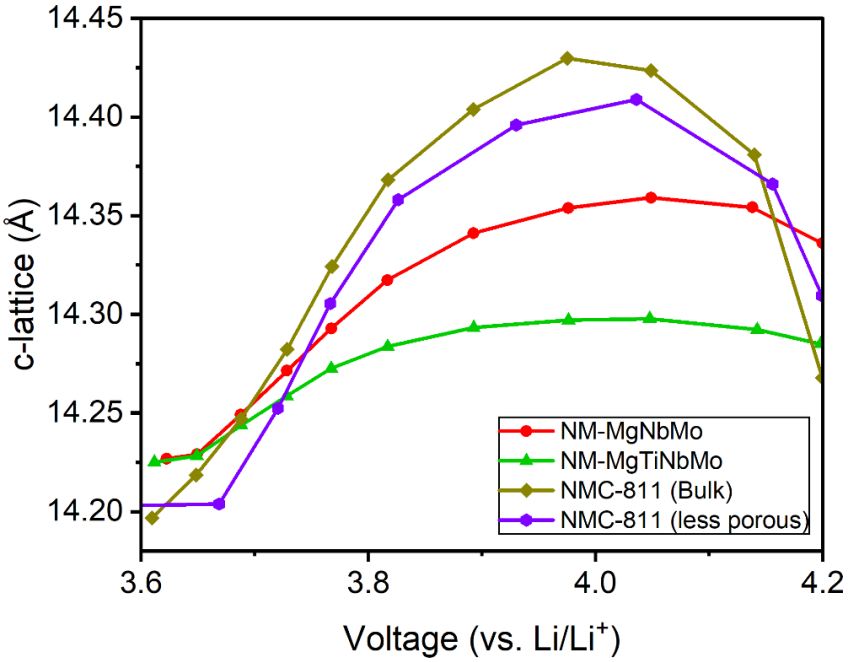

Figure 3.10: Fitted c-lattice parameters as a function of voltage during operando charging for NM-MgNbMo, NM-MgTiNbMo, bulk NMC-811, and less porous NMC-811.

The fitted c-lattice parameters in Figure 3.10 quantify the structural change across the measured charging range. NM-MgNbMo increases from approximately 14.23 Å to 14.36 Å near 4.05 V and then decreases to about 14.34 Å at 4.20 V. NM-MgTiNbMo increases from about 14.23 to 14.30 Å and ends near 14.29 Å. In comparison, bulk NMC-811 increases from approximately 14.20 to 14.43 Å before contracting to about 14.27 Å, while less porous NMC-811 reaches about 14.41 Å and ends near 14.31 Å. The total c-lattice ranges are therefore about 0.13 and 0.07 Å for NM-MgNbMo and NM-MgTiNbMo, compared with 0.23 and 0.21 Å for bulk and less porous NMC-811, respectively. The maximum-to-end contraction is only about 0.02 and 0.01 Å for the doped samples, compared with 0.16 Å for bulk NMC-811 and 0.10 Å for less porous NMC-811. Thus, the doped materials show both less c-lattice breathing across SOC and less collapse at the end

of charge.

The smaller c-lattice range indicates less c-axis breathing and a smaller strain change along the layered stacking direction, while the weak maximum-to-end contraction indicates suppressed high-SOC collapse. Within the present series, NM-MgTiNbMo has the greatest apparent cation disorder from the ex-situ XRD analysis and the smallest c-lattice range. This correlation is a finding of this thesis, not a conclusion established by the compositionally complex doping literature. Limited transition-metal occupancy in the Li layer may provide a local pillaring effect that constrains adjacent oxygen slabs, while multielement doping and Ti incorporation may also stabilize the local framework and distribute strain.[16,18,29]

The pillaring mechanism remains a hypothesis. Lee et al. electrochemically induced and quantified persistent bulk partial disorder in dopant-free $LiNi_{0.9}Mn_{0.1}O_2$, whereas the present apparent disorder is observed in the as-synthesized diffraction data and its exact location and concentration are not independently measured.[16] Zhang et al. demonstrated reduced strain in a compositionally complex cathode but did not establish cation disorder as the sole cause.[18] Excessive cation mixing can also obstruct Li^+ pathways, so more disorder is not necessarily beneficial.[28] Thus, the operando results are consistent with combined effects from dopant chemistry and controlled partial disorder, but they do not prove a specific pillaring structure. Reduced lattice breathing should lower the repeated strain that promotes particle cracking,[16,18] consistent with the cycling trends. However, dopant, disorder, and morphology effects cannot be separated here.

4. Conclusion

This thesis investigated nanostructuring and multi-element doping as a combined strategy for developing cobalt-free Ni-rich cathodes with improved fast-charging capability and structural stability. NM-MgNbMo, NM-MgAlMo, and NM-MgTiNbMo were synthesized using a polymer-assisted micelle-templated sol–gel method and compared with bulk and less porous NMC-811 references.

XRD and Rietveld refinement confirmed that all three doped materials retained the targeted layered α-$NaFeO_2$-type structure. The I(003)/I(104) ratios and calculated interlayer spacings were different and followed the order NM-MgNbMo > NM-MgAlMo > NM-MgTiNbMo. NM-MgNbMo therefore showed the least apparent cation mixing and the largest Li-layer spacing, providing a wider pathway for easier Li^+ transport and faster kinetics, whereas NM-MgTiNbMo showed the greatest mixing and the smallest spacing. These results identify partial disorder as a balance between a stabilizing pillaring effect and the preservation of open Li^+ pathways. This disorder–spacing relationship is a finding of the present thesis. SEM comparison showed that NM-MgNbMo formed an irregular, more open network of interconnected primary grains than the compact spherical secondary particles of bulk NMC-811.

NM-MgNbMo exhibited the best high-rate response among the doped samples and maintained approximately 36 mAh/g at 32C, while the capacity of bulk NMC-811 approached zero. Although less porous NMC-811 provided higher capacity at several low and moderate rates, all three doped materials performed favorably relative to the bulk reference. The CV analysis showed that NM-MgNbMo combined a high anodic *b*-value

with the smallest peak separation among the doped samples, consistent with favorable comparative kinetics during delithiation. The GITT comparison also showed a small apparent pulse-relaxation voltage difference. Because this voltage difference includes ohmic, charge-transfer, and solid-state transport contributions, it is interpreted as a comparative polarization metric rather than a direct Li^+ diffusion coefficient.

During long-term cycling, NM-MgNbMo retained the highest absolute capacity among the doped materials after 1000 cycles, whereas NM-MgTiNbMo retained the largest fraction of its lower initial capacity. Operando XRD showed that the doped materials underwent smaller c-lattice changes than the NMC-811 references, with NM-MgTiNbMo exhibiting the smallest variation. The combined results suggest a capacity-stability trade-off, although the individual effects of dopant chemistry, cation disorder, and particle morphology cannot be separated from the present data.

Overall, NM-MgNbMo provides the most balanced fast-charging response because it combines low apparent polarization with the highest high-rate capacity among the doped samples. NM-MgTiNbMo shows higher fractional retention and smaller c-lattice variation, but at the cost of lower accessible capacity. These results demonstrate that nanostructuring and dopant selection can provide complementary kinetic and structural advantages in Co-free Ni-rich cathodes.

5. References

[1] Kim, T.; Song, W.; Son, D.-Y.; Ono, L. K.; Qi, Y. Lithium-Ion Batteries: Outlook on Present, Future, and Hybridized Technologies. *J. Mater. Chem. A* **2019**, *7*, 2942–2964. https://doi.org/10.1039/C8TA10513H.

[2] Yang, J.; Liang, X.; Ryu, H.-H.; Yoon, C. S.; Sun, Y.-K. Ni-Rich Layered Cathodes for Lithium-Ion Batteries: From Challenges to the Future. *Energy Storage Mater.* **2023**, *63*, 102969. https://doi.org/10.1016/j.ensm.2023.102969.

[3] Wakihara, M. Recent Developments in Lithium Ion Batteries. *Mater. Sci. Eng., R* **2001**, *33*, 109–134. https://doi.org/10.1016/S0927-796X(01)00030-4.

[4] Manthiram, A. An Outlook on Lithium Ion Battery Technology. *ACS Cent. Sci.* **2017**, *3* (10), 1063–1069. https://doi.org/10.1021/acscentsci.7b00288.

[5] Blomgren, G. E. The Development and Future of Lithium Ion Batteries. *J. Electrochem. Soc.* **2017**, *164* (1), A5019–A5025. https://doi.org/10.1149/2.0251701jes.

[6] Manthiram, A. Materials Challenges and Opportunities of Lithium Ion Batteries. *J. Phys. Chem. Lett.* **2011**, *2* (3), 176–184. https://doi.org/10.1021/jz1015422.

[7] Ma, S.; Jiang, M.; Tao, P.; Song, C.; Wu, J.; Wang, J.; Deng, T.; Shang, W. Temperature Effect and Thermal Impact in Lithium-Ion Batteries: A Review. *Progress in Natural Science: Materials International* **2018**, *28* (6), 653–666. https://doi.org/10.1016/j.pnsc.2018.11.002.

[8] Tomaszewska, A.; Chu, Z.; Feng, X.; O'Kane, S.; Liu, X.; Chen, J.; Ji, C.; Endler, E.; Li, R.; Liu, L.; Li, Y.; Zheng, S.; Vetterlein, S.; Gao, M.; Du, J.; Parkes, M.; Ouyang, M.; Marinescu, M.; Offer, G.; Wu, B. Lithium-Ion Battery Fast Charging: A Review.

eTransportation **2019**, *1*, 100011. https://doi.org/10.1016/j.etran.2019.100011.

[9] Weiss, M.; Ruess, R.; Kasnatscheew, J.; Levartovsky, Y.; Levy, N. R.; Minnmann, P.; Stolz, L.; Waldmann, T.; Wohlfahrt-Mehrens, M.; Aurbach, D.; Winter, M.; Ein-Eli, Y.; Janek, J. Fast Charging of Lithium-Ion Batteries: A Review of Materials Aspects. *Adv. Energy Mater.* **2021**, *11* (33), 2101126. https://doi.org/10.1002/aenm.202101126.

[10] Xie, W.; Liu, X.; He, R.; Li, Y.; Gao, X.; Li, X.; Peng, Z.; Feng, S.; Feng, X.; Yang, S. Challenges and Opportunities toward Fast-Charging of Lithium-Ion Batteries. *J. Energy Storage* **2020**, *32*, 101837. https://doi.org/10.1016/j.est.2020.101837.

[11] Woo, Y. S.; Van Dyke, C. H.; Mardall, J.; Newport, C.; Ferguson, J. W. Cooling of Charging Cable. U.S. Patent 9,321,362 B2, April 26, 2016. https://patents.google.com/patent/US9321362B2/en.

[12] Mohamed, N.; Allam, N. K. Recent Advances in the Design of Cathode Materials for Li-Ion Batteries. *RSC Adv.* **2020**, *10*, 21662–21685. https://doi.org/10.1039/D0RA03314F.

[13] Murdock, B. E.; Toghill, K. E.; Tapia-Ruiz, N. A Perspective on the Sustainability of Cathode Materials Used in Lithium-Ion Batteries. *Adv. Energy Mater.* **2021**, *11* (39), 2102028. https://doi.org/10.1002/aenm.202102028.

[14] Noh, H.-J.; Youn, S.; Yoon, C. S.; Sun, Y.-K. Comparison of the Structural and Electrochemical Properties of Layered $Li[Ni_xCo_yMn_z]O_2$ (x = 1/3, 0.5, 0.6, 0.7, 0.8 and 0.85) Cathode Material for Lithium-Ion Batteries. *J. Power Sources* **2013**, *233*, 121–130. https://doi.org/10.1016/j.jpowsour.2013.01.063.

[15] Zhang, R.; Wang, C.; Zou, P.; Lin, R.; Ma, L.; Li, T.; Hwang, I.; Xu, W.; Sun, C.; Trask, S.; Xin, H. L. Long-Life Lithium-Ion Batteries Realized by Low-Ni, Co-Free

Cathode Chemistry. *Nat. Energy* **2023**, *8* (7), 695–702. https://doi.org/10.1038/s41560-023-01267-y.

[16] Lee, J.; Jiang, Z.; Liang, N. B.; Kwak, J. H.; Nguyen, H.; Busse, G. M.; Yoo, Y.; Ramachandran, H.; Lim, K.; Csernica, P. M.; Li, T.; Xu, X.; Chung, K. Y.; Michel, K.; Frerichs, J. E.; Gent, W. E.; Clément, R. J.; Park, J.; Chueh, W. C. Eliminating Lattice Collapse in Dopant-Free $LiNi_{0.9}Mn_{0.1}O_2$ Cathodes via Electrochemically Induced Partial Cation Disorder. *Nat. Energy* **2026**, *11*, 87–97. https://doi.org/10.1038/s41560-025-01910-w.

[17] Tang, Y.; Wang, X.-Y.; Ren, J.-C.; Chen, B.-W.; Huang, Z.-Y.; Wang, W.; Huang, Y.-L.; Zhang, B.-H.; Lan, S.; He, Z.-L.; Liu, Q.; He, H. Insight into Structural Degradation of NCMs under Extreme Fast Charging Process. *Rare Met.* **2024**, *43*, 41–50. https://doi.org/10.1007/s12598-023-02454-2.

[18] Zhang, R.; Wang, C.; Zou, P.; Lin, R.; Ma, L.; Yin, L.; Li, T.; Xu, W.; Jia, H.; Li, Q.; Sainio, S.; Kisslinger, K.; Trask, S. E.; Ehrlich, S. N.; Yang, Y.; Kiss, A. M.; Ge, M.; Polzin, B. J.; Lee, S. J.; Xu, W.; Ren, Y.; Xin, H. L. Compositionally Complex Doping for Zero-Strain Zero-Cobalt Layered Cathodes. *Nature* **2022**, *610*, 67–73. https://doi.org/10.1038/s41586-022-05115-z.

[19] Zhou, J.; Hu, J.; Zhou, X.; Shang, Z.; Yang, Y.; Xu, S. High-Entropy Doping for High-Performance Zero-Cobalt High-Nickel Layered Cathode Materials. *Energy Environ. Sci.* **2025**, *18* (1), 347–353. https://doi.org/10.1039/D4EE05020G.

[20] Zhang, B.; Zhang, H.; Su, Y.; Dong, J.; Yan, K.; Liu, J.; Lu, Y.; Wang, H.; Wang, C.; Wu, F.; Chen, L. Rare-Earth Doping Induced Pinning Effect with Enhanced Chemo-

Mechanical Stability in Ni-Rich Cathodes for Lithium-Ion Batteries. *Chin. J. Chem.* **2025**, *43* (8), 889–896. https://doi.org/10.1002/cjoc.202401071.

[21] Pitchai, R.; Thavasi, V.; Mhaisalkar, S. G.; Ramakrishna, S. Nanostructured Cathode Materials: A Key for Better Performance in Li-Ion Batteries. *J. Mater. Chem.* **2011**, *21*, 11040–11051. https://doi.org/10.1039/C1JM10857C.

[22] Basile, V. M.; Lai, C.-H.; Kim, G. Y.; Choi, C. S.; Butts, D. M.; Thurber, K.; King, S. C.; Tolbert, S. H. Nanostructured $LiNi_{0.80}Co_{0.15}Al_{0.05}O_2$ (NCA) for Fast-Charging, High-Capacity Battery Cathodes. *Nanoscale Horiz.* **2025**, *10*, 3013–3028. https://doi.org/10.1039/D5NH00290G.

[23] Uddin, M.-J.; Alaboina, P. K.; Cho, S.-J. Nanostructured Cathode Materials Synthesis for Lithium-Ion Batteries. *Mater. Today Energy* **2017**, *5*, 138–157. https://doi.org/10.1016/j.mtener.2017.06.008.

[24] Augustyn, V.; Come, J.; Lowe, M. A.; Kim, J. W.; Taberna, P.-L.; Tolbert, S. H.; Abruña, H. D.; Simon, P.; Dunn, B. High-Rate Electrochemical Energy Storage through Li^+ Intercalation Pseudocapacitance. *Nat. Mater.* **2013**, *12* (6), 518–522. https://doi.org/10.1038/nmat3601.

[25] Kim, H.-S.; Cook, J. B.; Tolbert, S. H.; Dunn, B. The Development of Pseudocapacitive Properties in Nanosized-MoO_2. *J. Electrochem. Soc.* **2015**, *162* (5), A5083–A5090. https://doi.org/10.1149/2.0141505jes.

[26] Simon, P.; Gogotsi, Y.; Dunn, B. Where Do Batteries End and Supercapacitors Begin? *Science* **2014**, *343* (6176), 1210–1211. https://doi.org/10.1126/science.1249625.

[27] Toby, B. H.; Von Dreele, R. B. GSAS-II: The Genesis of a Modern Open-Source All-

Purpose Crystallography Software Package. *J. Appl. Crystallogr.* **2013**, *46*, 544–549. https://doi.org/10.1107/S0021889813003531.

[28] Li, J.; Liang, G.; Zheng, W.; Zhang, S.; Davey, K.; Pang, W. K.; Guo, Z. Addressing Cation Mixing in Layered Structured Cathodes for Lithium-Ion Batteries: A Critical Review. *Nano Mater. Sci.* **2023**, *5*, 404–420. https://doi.org/10.1016/j.nanoms.2022.09.001.

[29] Kim, J.-H.; Kim, H.; Kim, W.-J.; Kim, Y.-C.; Jung, J.-Y.; Rhee, D.-Y.; Song, J.-H.; Cho, W.; Park, M.-S. Incorporation of Titanium into Ni-Rich Layered Cathode Materials for Lithium-Ion Batteries. *ACS Appl. Energy Mater.* **2020**, *3* (12), 12204–12211. https://doi.org/10.1021/acsaem.0c02258.

[30] Lindström, H.; Södergren, S.; Solbrand, A.; Rensmo, H.; Hjelm, J.; Hagfeldt, A.; Lindquist, S.-E. Li^+ Ion Insertion in TiO_2 (Anatase). 2. Voltammetry on Nanoporous Films. *J. Phys. Chem. B* **1997**, *101* (39), 7717–7722. https://doi.org/10.1021/jp970490q.

[31] Horner, J. S.; Whang, G.; Ashby, D. S.; Kolesnichenko, I. V.; Lambert, T. N.; Dunn, B. S.; Talin, A. A.; Roberts, S. A. Electrochemical Modeling of GITT Measurements for Improved Solid-State Diffusion Coefficient Evaluation. *ACS Appl. Energy Mater.* **2021**, *4* (10), 11460–11469. https://doi.org/10.1021/acsaem.1c02218.

[32] Kang, K.; Ceder, G. Factors That Affect Li Mobility in Layered Lithium Transition Metal Oxides. *Phys. Rev. B* **2006**, *74* (9), 094105. https://doi.org/10.1103/PhysRevB.74.094105.

[33] Kondrakov, A. O.; Geßwein, H.; Galdina, K.; De Biasi, L.; Meded, V.; Filatova, E. O.; Schumacher, G.; Wenzel, W.; Hartmann, P.; Brezesinski, T.; Janek, J. Charge-Transfer-

Induced Lattice Collapse in Ni-Rich NCM Cathode Materials during Delithiation. *J. Phys. Chem. C* **2017**, *121* (44), 24381–24388. https://doi.org/10.1021/acs.jpcc.7b06598.